Model-Based Iterative Reconstruction for Synchrotron X-Ray Tomography

K. Aditya Mohan*, S. V. Venkatakrishnan*, Lawrence F. Drummy ‡, Jeff Simmons ‡, Dilworth Y. Parkinson†, and Charles A. Bouman*

*School of Electrical and Computer Engineering, Purdue University, West Lafayette, IN, 47907, USA
† Advanced Light Source, Lawrence Berkeley National Laboratory, Berkeley, California 94720, USA
‡ Air Force Research Laboratory, Dayton, OH, USA

Abstract—**Synchrotron based X-ray tomography is widely used for three dimensional imaging of materials at the micron scale. Tomographic data collected from a synchrotron is often affected by non-idealities in the measurement system and sudden "blinding" of detector pixels during the acquisition. Typically, reconstructions are done using analytical reconstruction techniques combined with pre/post-processing steps to correct for the non-idealities, resulting in loss of detail while still producing noisy reconstructions with some artifacts.**

In this paper, we present a model-based iterative reconstruction (MBIR) algorithm for synchrotron X-ray tomography that can automatically handle the non-idealities as a part of the reconstruction. First, we develop a forward model that accounts for the non-idealities in the measurement system and for the occurrence of outliers in the measurement. Next, we combine the forward model with a prior model of the object to formulate the MBIR cost function and propose an algorithm to minimize the cost. Results on a real data set show that the MBIR reconstructions are superior to the analytical reconstructions effectively suppressing noise as well as other artifacts.

I. INTRODUCTION

Synchrotron based X-rays are used for fast 3D imaging of a wide range of specimens in applications ranging from biology [1] to material science [2]. Due to the high intensity and strong collimation of synchrotron radiation, it is possible to select the optimal photon energy using monochromators thereby enabling a variety of samples to be imaged [3]. For tomography, the sample is mounted on a rotating stage, radiated with a parallel beam of X-rays and repeatedly imaged at different views, typically using a scintillator and CCD detector. However, tomographic reconstructions of the acquired data is challenging because of impurities in the scintillator crystal, dust in the scintillator screens and imperfections in the detector elements which introduce differences in gain at different positions along the detector array [3], [4]. Furthermore, detector pixels get occasionally saturated by high energy photons (often called *zingers*), making it difficult to directly use the measurements for reconstruction. Thus, while synchrotron microtomography is widely used, tomographic

inversion is challenging due to the nature of the detectors and the varying imaging conditions.

In synchrotron based microtomography, analytical reconstruction algorithms such as filtered back projection (FBP) or related methods like *gridrec* [5] are the dominant choice for tomographic reconstruction [2], [6]. These algorithms typically require data to be acquired at a large number of views [7] for an accurate reconstruction. Furthermore, when these algorithms are directly applied to the data, the zingers result in streaks in the reconstruction while the imperfections in the detector and scintillator manifest as rings of varying size and intensity. In the literature, several works have addressed the problem of removal of ring artifacts and zingers either as a pre-processing step on the sinogram [8], [9] or as a post-processing step on the reconstructions [4]. However, these require manual intervention and can result in loss of detail in the reconstruction. Thus, the typical tomographic inversion for synchrotron microtomography involves a few steps of pre/post-processing along with an analytical reconstruction technique.

In this paper, we present a model-based iterative reconstruction (MBIR) [10]–[12] algorithm which can handle the anomalies in the data as a part of the tomographic reconstruction. First, we develop a forward model (likelihood function) that accounts for the non-uniformities in the measurement system as well as the presence of outliers (zingers) in the measurement. Modeling the measurement non-uniformities and presence of outliers, requires certain calibration parameters that are typically not measured. Hence we treat them as "nuisance" parameters and include their estimation as a part of the reconstruction. Next, we combine the forward model with a prior model for the object to formulate the MBIR cost function and develop a computationally efficient algorithm based on functional substitution [13], [14] to minimize it. Reconstructions on a real data set suggest that the proposed MBIR algorithm can significantly improve the quality of reconstruction even with reduced view data sets, effectively suppressing noise as well as streaks and ring artifacts.

II. FORMULATION OF MBIR COST FUNCTION

In MBIR, the reconstruction is typically formulated as the maximum *a posteriori* (MAP) estimate of the unknowns given the data. If y represents the data, x represents the unknown voxels and ϕ represents the unknown calibration parameters associated with the measurement, then the reconstruction is
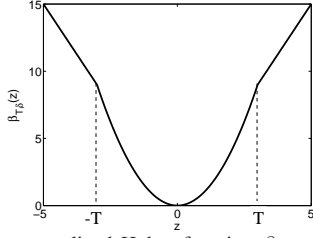
Fig. 1. Plot of the generalized Huber function $\beta_{T,\delta}$ used in the likelihood term with $T = 3$ and $\delta = \frac{1}{2}$. Projections with large data mismatch error are penalized thereby reducing their influence in the overall cost function.

given by

$$(\hat{x}, \hat{\phi}) = \underset{x,\phi}{\operatorname{argmin}}\{-\log p(y|x, \phi) - \log p(x)\} \tag{1}$$

where we have assumed a uniform prior for the unknown calibration parameters.

We begin by developing a likelihood function $p(y|x, \phi)$ for the synchrotron data that models the measurement variations and the presence of zingers. A widely used model for X-ray transmission measurements is based on Beer's law along with Poisson counting statistics for the measurement [15]. Using this model, if $\lambda_{n,i}$ is the photon count at the ith detector element and n^{th} view and $\lambda_{D,i}$ is the photon count measured in the absence of the sample, then an estimate of the projection integral is given by $y_{n,i} = \log\left(\frac{\lambda_{D,i}}{\lambda_{n,i}}\right)$. If we denote y to be the vector of projections $y_{n,i}$ and x to be the vector of attenuation coefficients, then it has been shown [16] that using a Taylor series approximation to the Poisson log-likelihood function,

$$-\log p(y|x) \approx \frac{1}{2}\sum_{n=1}^{N}\sum_{i=1}^{M}\left((y_{n,i} - A_{n,i,*}x)\frac{\sqrt{\Lambda_{n,i,i}}}{\sigma}\right)^2 + f(y) \tag{2}$$

where $A_{n,i,*}$ is the ith row of the forward projection matrix A_n, Λ_n is a diagonal matrix such that $\frac{\Lambda_{n,i,i}}{\sigma^2}$ is the inverse variance of the projection measurement $y_{n,i}$, σ^2 is a proportionality constant, N is the total number of views, M is the total number of detector elements and $f(y)$ is a constant which is ignored in the subsequent optimization. The variance of projection measurement is inversely proportional to the mean photon counts and hence we can set $\Lambda_{n,i,i} = \lambda_{n,i}$ [15].

While this model is useful in several applications, it does not take into account the non-uniformities in the measurement system (that typically result in rings in the reconstruction) and presence of zingers in the synchrotron microtomography measurements. The log-likelihood term in (2) corresponds to a quadratic penalty on the weighted data mismatch error and does not account for the occurrence of anomalies in the measurement [11]. The occurrence of zingers corresponds to a distribution with heavier tails than those corresponding to (2). Hence we change the quadratic penalty to a *generalized* Huber penalty (see Fig. 1) of the form

$$\beta_{T,\delta}(z) = \begin{cases} z^2 & |z| < T \\ 2\delta T|z| + T^2(1 - 2\delta) & |z| \geq T \end{cases}$$

The function $\beta_{T,\delta}$ reduces to the Huber function [17] when $\delta = 1$ and to the weak-spring potential [18] when $\delta = 0$.

Intuitively, this penalty implies that if the ratio of the data mismatch error to the noise standard deviation is greater than a threshold T then the measured projection corresponds to a zinger. Next, we model the influence of non-idealities in the measurement system. It has been shown [19] that the non-idealities that cause ring artifacts can be modeled via an additive detector dependent offset to the projection measurements. Hence we assume a detector dependent offset d_i in all the projections measured by detector i. This value is typically not known from the measurements and hence we jointly estimate it as a part of the reconstruction. Combining the new penalty term along with the detector dependent offset gives us a new log-likelihood function,

$$-\log p(y|x, d, \sigma) =$$
$$\frac{1}{2}\sum_{n=1}^{N}\sum_{i=1}^{M}\beta_{T,\delta}\left((y_{n,i} - A_{n,i,*}x - d_i)\frac{\sqrt{\Lambda_{n,i,i}}}{\sigma}\right)$$
$$+ MN\log(\sigma) + \tilde{f}(y) \tag{3}$$

where $d = [d_1 \cdots d_M]$, and $\tilde{f}(y)$ is a constant which is ignored in the subsequent optimization. We note that when $\delta = 0$, $p(y|x, d, \sigma)$ is not a density function since it does not integrate to 1 and hence we assume $\delta > 0$ in the rest of the paper.

We use a special case of the q-generalized Gaussian Markov Random Field (qGGMRF) [20] as a prior model for the voxels. The density function corresponding to this prior is given by

$$p(x) = \frac{1}{Z}\exp\left\{-\sum_{\{j,k\}\in\mathcal{N}} w_{jk}\rho(x_j - x_k)\right\} \tag{4}$$

$$\rho(x_j - x_k) = \frac{\Delta_s^3 \left|\frac{x_j - x_k}{\Delta_s \sigma_s}\right|^2}{c + \left|\frac{x_j - x_k}{\Delta_s \sigma_s}\right|^{2-p}}$$

where Z is a normalizing constant, Δ_s is the side length of a voxel, $\mathcal{N}$ is the set of all pairwise cliques (all pairs of neighbors in a 26 point neighborhood system), p, c and σ_s are qGGMRF parameters. The weights w_{jk} are set to be inversely proportional to the distance between voxels j and k, normalized to 1. The term Δ_s in the model ensures invariance of the prior to changing voxel sizes [21].

Substituting (3) and (4) into (1), the reconstruction is obtained by jointly minimizing the following cost function with respect to x, d and σ,

$$c(x, d, \sigma) = \frac{1}{2}\sum_{n=1}^{N}\sum_{i=1}^{M}\beta_{T,\delta}\left((y_{n,i} - A_{n,i,*}x - d_i)\frac{\sqrt{\Lambda_{n,i,i}}}{\sigma}\right)$$
$$+ MN\log(\sigma) + \sum_{\{j,k\}\in\mathcal{N}} w_{jk}\rho(x_j - x_k) \tag{5}$$

III. OPTIMIZATION ALGORITHM

The cost function (5) is in general non-convex in x, d and σ. Thus, the optimization algorithm developed in this paper converges to a local minimum of (5). Minimizing the current form of the cost function given by (5) is computationally expensive. So, instead we use the functional substitution

approach [13], [14] to efficiently minimize (5). Our method also ensures monotonic decrease of the cost function (5). A substitute function $c_{\text{sub}}(x, d, \sigma; x', d', \sigma')$ to the cost function $c(x, d, \sigma)$ at the point (x', d', σ') is a function which upper bounds the cost function such that minimizing the substitute function results in a lower value of the original cost function.

A. Construction of Substitute Function

To derive a substitute function to the overall cost we find a substitute function to each term of the cost (5) and sum them together to derive an overall substitute function. In particular, we will use quadratic substitute functions, as they make the subsequent optimization computationally simple. A sufficient condition for a function $q(z; z')$ to be a substitute function to $g(z)$ at the point z' is that $\forall z$,

$$
\begin{aligned}
q(z; z') &\geq g(z) \\
q(z'; z') &= g(z')
\end{aligned}
$$

We can then show that

$$
Q_{T,\delta}(z; z') = \begin{cases} z^2 & |z'| < T \\ \frac{\delta T}{|z'|} z^2 + \delta T |z'| + T^2 (1 - 2\delta) & |z'| \geq T \end{cases}
$$

is a substitute function to $\beta_{T,\delta}(z)$ by showing that it satisfies the sufficiency condition. If the error sinogram is defined as $e_{n,i} = y_{n,i} - A_{n,i,*}x - d_i$ and $e'_{n,i} = y_{n,i} - A_{n,i,*}x' - d'_i$ is the error sinogram at the current values of (x', d', σ'), then a substitute function to the term $\beta_{T,\delta}\left(e_{n,i}\sqrt{\Lambda_{n,i,i}}/\sigma\right)$ in the original cost is given by $Q_{T,\delta}\left(e_{n,i}\sqrt{\Lambda_{n,i,i}}/\sigma; e'_{n,i}\sqrt{\Lambda_{n,i,i}}/\sigma'\right)$ by Property 7.9 in [22].

A quadratic substitute function for the prior term $\rho(x_j - x_k)$ can be shown to be [10]

$$
\rho(x_j - x_k; x'_j - x'_k) = \frac{a_{jk}}{2}(x_j - x_k)^2 + b_{jk}. \quad (6)
$$

$$
\text{where } a_{jk} = \begin{cases} \frac{\rho'(x'_j - x'_k)}{(x'_j - x'_k)} & x'_j \neq x'_k \\ \rho''(0) & x'_j = x'_k \end{cases} \quad (7)
$$

$$
b_{jk} = \rho(x'_j - x'_k) - \frac{a_{jk}}{2}(x'_j - x'_k)^2 \quad (8)
$$

Thus, a substitute function to (5) is given by

$$
c_{\text{sub}}(x, d, \sigma; x', d', \sigma') =
$$

$$
\frac{1}{2} \sum_{n=1}^{N} \sum_{i=1}^{M} Q_{T,\delta}\left(e_{n,i}\frac{\sqrt{\Lambda_{n,i,i}}}{\sigma}; e'_{n,i}\frac{\sqrt{\Lambda_{n,i,i}}}{\sigma'}\right)
$$

$$
+ MN \log(\sigma) + \sum_{\{j,k\} \in \mathcal{N}} w_{jk}\rho(x_j - x_k; x'_j - x'_k) \quad (9)
$$

B. Parameter Updates used in Optimization

To minimize the cost function given by (5), we repeatedly construct and minimize (9) w.r.t. each voxel, the offset error parameters and the variance parameter σ.

To simplify the updates, we define $b'_{n,i}$ to be a indicator variable which classifies measurements as anomalous based on the current error, $e'_{n,i}$, and σ', as shown below,

$$
b'_{n,i} = \begin{cases} 1 & \left|e'_{n,i}\sqrt{\Lambda_{n,i,i}}/\sigma'\right| < T \\ 0 & \left|e'_{n,i}\sqrt{\Lambda_{n,i,i}}/\sigma'\right| \geq T \end{cases} \quad (10)
$$

1) Voxel Update: In order to minimize (9) with respect to a voxel j, we take derivative of (9) with respect to x_j and set it to 0. This gives the optimal update for pixel j as

$$
\hat{x}_j = \frac{\displaystyle\sum_{k \in \mathcal{N}_j} w_{jk}a_{jk}x'_k + \tilde{\theta}_2 x'_j + \tilde{\theta}_1}{\displaystyle\sum_{k \in \mathcal{N}_j} w_{jk}a_{jk} + \tilde{\theta}_2},
$$

where $\mathcal{N}_j$ is the set of all neighbors of voxel j and $\tilde{\theta}_1 =$

$$
\sum_{n=1}^{N} \sum_{i=1}^{M} A_{n,i,j} \frac{\sqrt{\Lambda_{n,i,i}}}{\sigma'} \left[b'_{n,i}e'_{n,i}\frac{\sqrt{\Lambda_{n,i,i}}}{\sigma'} + (1 - b'_{n,i})\delta T \mathrm{sgn}(e'_{n,i}) \right]
$$

$$
\tilde{\theta}_2 = \sum_{n=1}^{N} \sum_{i=1}^{M} A_{n,i,j}^2 \frac{\sqrt{\Lambda_{n,i,i}}}{\sigma'} \left[b'_{n,i}\frac{\sqrt{\Lambda_{n,i,i}}}{\sigma'} + (1 - b'_{n,i})\frac{\delta T}{|e'_{n,i}|} \right]
$$

and sgn is the *signum* function.

2) Offset Error and Variance Parameter Update: In order to minimize (9) with respect to the offset error parameter d, we take the gradient of the substitute function (9) with respect to d and set it to zero. This gives the optimal update for d_i as

$$
\hat{d}_i = d'_i + \frac{\displaystyle\sum_{n=1}^{N} \left[e'_{n,i}b'_{n,i}\frac{\sqrt{\Lambda_{n,i,i}}}{\sigma'} + \delta T \mathrm{sgn}(e'_{n,i})(1 - b'_{n,i}) \right]}{\displaystyle\sum_{n=1}^{N} \left[b'_{n,i}\frac{\sqrt{\Lambda_{n,i,i}}}{\sigma'} + \frac{\delta T}{|e'_{n,i}|}(1 - b'_{n,i}) \right]}
$$

The update for the variance parameter, σ^2, is obtained by taking the derivative of (9) with respect to σ^2 and setting it to zero. The update is then given by,

$$
\hat{\sigma}^2 = \frac{1}{NM} \sum_{n=1}^{N} \sum_{i=1}^{M} \left[e'^2_{n,i}\Lambda_{n,i,i}b'_{n,i} \right.
$$

$$
\left. + (1 - b'_{n,i})\delta T \left|e'_{n,i}\right| \sigma'\sqrt{\Lambda_{n,i,i}} \right]
$$

Finally, to improve convergence, we implemented Non-Homogeneous Iterative Coordinate Descent (NHICD) [10] which works by more frequently updating those voxels which have a greater need for updates. Furthermore, we use a multi-resolution initialization [23] which performs reconstructions at coarser resolutions and uses that to initialize the reconstruction at a finer resolution. We also parallelize the voxel updates across slices (along axis parallel to axis of rotation) using multi-threaded shared memory parallelization similar to [24].

IV. EXPERIMENTAL RESULTS

In this section, we will compare MBIR reconstructions with an analytical reconstruction technique called *gridrec* (GR) [5], which is a Fourier domain interpolation based algorithm, widely used for synchrotron tomography. To illustrate the removal of ring artifacts and streaks caused by zingers, we will compare the proposed MBIR algorithm (MBIR-RZ) to the conventional MBIR algorithm (MBIR-CV) which is based on the model in (2). We also compare MBIR-RZ with a pre/post-processed version of *gridrec* (GR-PP) where zingers are removed via median filtering in the sinogram domain, after

(a) Conventional *gridrec* (GR)

(b) Conventional MBIR (MBIR-CV)

(c) Corrected *gridrec* (GR-PP)
Noise = 2.06cm^{-1}

(d) Proposed MBIR (MBIR-RZ)
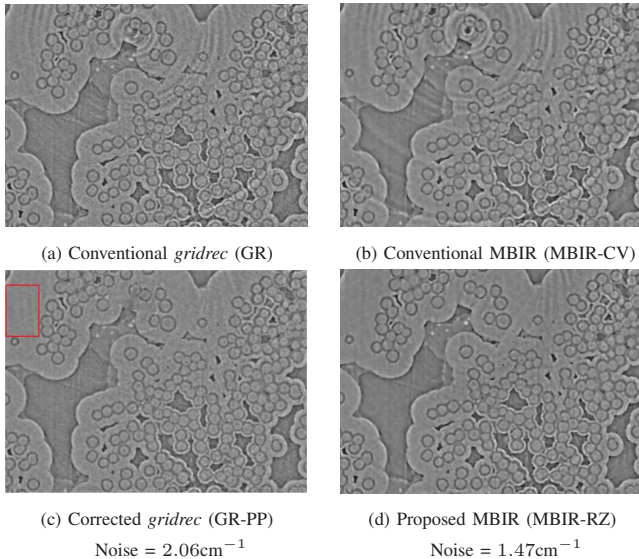Noise = 1.47cm^{-1}

Fig. 2. A single reconstructed slice showing the quality improvements of MBIR over *gridrec* for a data set with 1024 views. (a) Conventional *gridrec* reconstruction without any post-processing (GR). (b) Conventional MBIR reconstruction without modeling the zingers and non-idealities in the measurement system (MBIR-CV). (c) *Gridrec* reconstruction with pre/post-processing to remove zingers and rings (GR-PP). (d) Proposed MBIR (MBIR-RZ). Reconstruction using MBIR-RZ as shown in (d) has sharper features and lesser noise than GR-PP as shown in (c). The noise standard deviation is calculated within the red colored rectangular box shown in (c). By comparing the images, we can conclude that MBIR-RZ suppresses the ring artifacts while preserving detail and reducing noise. All images are displayed using the same viewing window.

which the volume is reconstructed and rings are removed using [25]. We reconstruct a ceramic composite material [2] imaged using synchrotron X-ray radiation. During the experiment, projections were acquired at 1024 different views around the object. All the reconstructions are of size 2560×2560 in the plane perpendicular to the rotation axis and have a voxel size of $0.65\mu m^3$. The parameter p of the qGGMRF prior model is set to 1.2, and σ_s is chosen to give the best visual quality of the reconstructed image. The parameters of the generalized Huber function are chosen to be $\delta = 0.05$ and $T = 3.5$. All figures in this section show a zoomed in portion of the original reconstructed slice.

First, we reconstruct the volume using the full set of 1024 views. The ring artifacts are prominent in reconstructions obtained using GR and MBIR-CV as shown in Fig. 2 (a), (b). We notice that while MBIR-CV better preserves the edges it also sharpens the ring artifacts, emphasizing the need for accurate system modeling. However, the proposed MBIR-RZ (Fig. 2(d)) preserves the edges and reduces the noise when compared to GR-PP (Fig. 2(c)), while significantly reducing the ring artifacts.

Next, we reconstruct the volume but only using 128 equally spaced views. Reducing the views can be beneficial in a synchrotron setting because it can enable faster acquisitions and improve the temporal resolution of *in-situ* experiments which are increasing in popularity. In this case the *gridrec* reconstructions (Fig. 3 (a) and (c)) are very noisy and do not reconstruct the object with sufficient detail. MBIR-CV (Fig. 3 (b)) preserves most of the details but has ring artifacts and

(a) Conventional *gridrec* (GR)

(b) Conventional MBIR (MBIR-CV)

(c) Pre/post-processed *gridrec* (GR-PP)
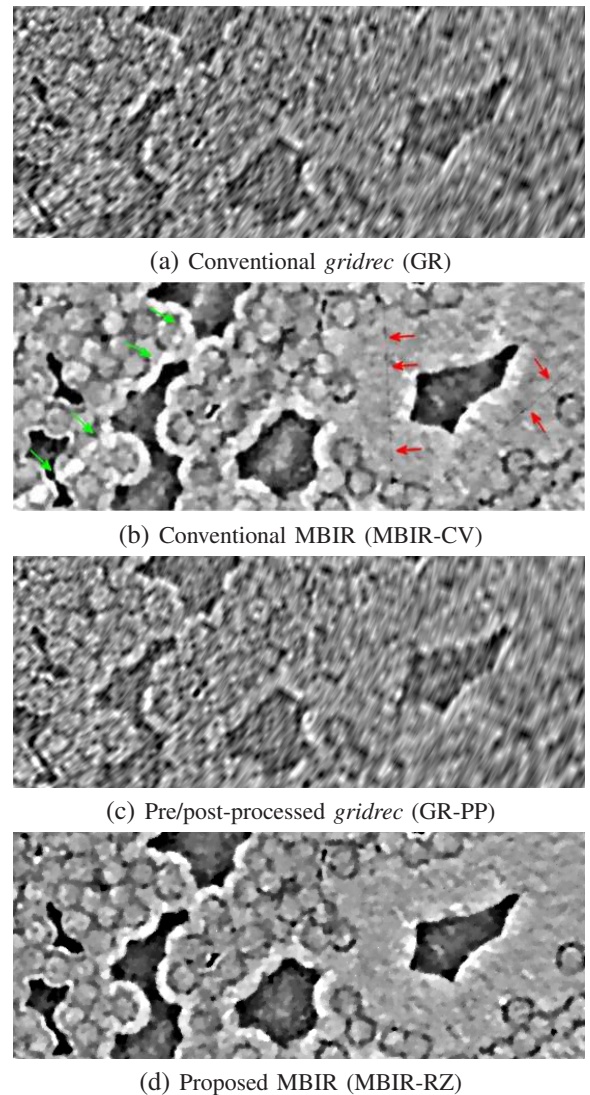
(d) Proposed MBIR (MBIR-RZ)

Fig. 3. Illustration of the effect on reconstruction quality by using projections from 128 views. (a) Conventional *gridrec* (GR). (b) Conventional MBIR without modeling the zingers and non-idealities in the measurement system (MBIR-CV). (c) *gridrec* reconstruction with pre/post-processing to remove zingers and rings (GR-PP). (d) Proposed MBIR (MBIR-RZ). In (b), we can clearly see the ring artifacts (shown using green arrows) and streaks caused by zingers (shown using red arrows). Notice that MBIR-RZ better suppresses the streaks and ring artifacts compared to other methods.

streaks (these were less pronounced in Fig. 2 due to the large number of views acquired). However, MBIR-RZ (Fig. 3 (d)) suppresses the streaks due to zingers and also removes the ring artifacts, while preserving the details in the reconstruction.

V. CONCLUSIONS

In this paper, we presented a MBIR algorithm for synchrotron X-ray tomography which incorporates a model for the anomalous measurements (zingers) and non-idealities in the measurement system. Reconstructions on real data shows the effectiveness of our algorithm in suppressing ring artifacts and streaks while retaining sharpness and lowering noise even when using fewer views than is typically acquired.

REFERENCES

[1] R. Mizutani and Y. Suzuki, "X-ray microtomography in biology," *Micron*, vol. 43, no. 23, pp. 104 – 115, 2012.

[2] H. A. Bale, A. Haboub, A. A. MacDowell, J. R. Nasiatka, D. Y. Parkinson, B. N. Cox, D. B. Marshall, and R. O. Ritchie, "Real-time quantitative imaging of failure events in materials under load at temperatures above 1,600° C," *Nature Materials*, vol. 12, no. 1, 2013.

[3] T. Donath, "Quantitative X-ray microtomography with synchrotron radiation," Ph.D. dissertation, GKSS-Forschungszentrum, 2007.

[4] J. Sijbers and A. Postnov, "Reduction of ring artifacts in high resolution micro-CT reconstructions," *Physics in Medicine and Biology*, vol. 49, no. 14, p. N247.

[5] F. Marone and M. Stampanoni, "Regridding reconstruction algorithm for real-time tomographic imaging," *Journal of Synchrotron Radiation*, vol. 19, no. 6, pp. 1029–1037, Nov 2012.

[6] F. Fusseis, K. Regenauer-Lieb, J. Liu, R. M. Hough, and F. D. Carlo, "Creep cavitation can establish a dynamic granular fluid pump in ductile shear zones," *Nature*, vol. 459, no. 7249, pp. 974–977, 2009.

[7] A. C. Kak and M. Slaney, *Principles of Computerized Tomographic Imaging*. Philadephia, PA: Society for Industrial and Applied Mathematics, 2001.

[8] M. Rivers, "Tutorial introduction to X-ray computed microtomography data processing," 1998. [Online]. Available: http://www.mcs.anl.gov/research/projects/X-ray-cmt/rivers/tutorial.html

[9] R. Ketcham, "New algorithms for ring artifact removal," *Proc SPIE*, vol. 6318, no. 4, pp. 6 318 001–6 318 007, 2006.

[10] Z. Yu, J. Thibault, C. Bouman, K. Sauer, and J. Hsieh, "Fast model-based X-ray CT reconstruction using spatially nonhomogeneous ICD optimization," *IEEE Trans. on Image Processing*, vol. 20, no. 1, pp. 161 –175, Jan. 2011.

[11] S. V. Venkatakrishnan, L. F. Drummy, M. De Graef, J. P. Simmons, and C. A. Bouman, "Model based iterative reconstruction for bright field electron tomography," *Proc. SPIE 8657, Computational Imaging XI, 86570A (February 14, 2013)*, pp. 86 570A–86 570A–12, 2013.

[12] J. Fessler, "Penalized weighted least-squares image reconstruction for positron emission tomography," *IEEE Trans. on Medical Imaging*, vol. 13, no. 2, pp. 290 –300, Jun. 1994.

[13] J. Zheng, S. Saquib, K. Sauer, and C. Bouman, "Parallelizable Bayesian tomography algorithms with rapid, guaranteed convergence," *Image Processing, IEEE Transactions on*, vol. 9, no. 10, pp. 1745–1759, 2000.

[14] H. Erdogan and J. Fessler, "Monotonic algorithms for transmission tomography," *Medical Imaging, IEEE Transactions on*, vol. 18, no. 9, pp. 801–814, 1999.

[15] K. Sauer and C. Bouman, "Bayesian Estimation of Transmission Tomograms Using Segmentation Based Optimization," *IEEE Trans. on Nuclear Science*, vol. 39, pp. 1144–1152, 1992.

[16] C. Bouman and K. Sauer, "A unified approach to statistical tomography using coordinate descent optimization," *IEEE Trans. on Image Processing*, vol. 5, no. 3, pp. 480 –492, Mar. 1996.

[17] R. L. Stevenson and E. J. Delp, "Fitting curves with discontinuities," in *Proc. of the first IEEE Int. Workshop on Robust Computer Vision*, Oct. 1990, pp. 127–136.

[18] A. Blake, "Comparison of the efficiency of deterministic and stochastic algorithms for visual reconstruction," *IEEE Trans. Pattern Anal. Mach. Intell.*, vol. 11, no. 1, pp. 2–12, Jan. 1989.

[19] J. Hsieh, *Computed Tomography: Principles, Design, Artifacts, and Recent Advances,*. SPIE Press, Nov. 2009.

[20] J.-B. Thibault, K. D. Sauer, C. A. Bouman, and J. Hsieh, "A three-dimensional statistical approach to improved image quality for multislice helical CT," *Medical Physics*, vol. 34, no. 11, pp. 4526–4544, 2007.

[21] S. Oh, A. Milstein, C. Bouman, and K. Webb, "A general framework for nonlinear multigrid inversion," *Image Processing, IEEE Transactions on*, vol. 14, no. 1, pp. 125–140, 2005.

[22] C. A. Bouman, *Model Based Image And Signal Processing*, 2013.

[23] M. Kamasak, C. Bouman, E. Morris, and K. Sauer, "Direct reconstruction of kinetic parameter images from dynamic PET data," *IEEE Trans. on Medical Imaging*, vol. 24, no. 5, pp. 636 –650, May 2005.

[24] P. Jin, E. Haneda, K. Sauer, and C. A. Bouman, "A Model-Based 3D Multi-slice Helical CT Reconstruction Algorithm for Transportation Security Application," in *Second International Conference on Image Formation in X-Ray Computed Tomography*, Salt Lake City, Utah, USA, Jun. 2012.

[25] D. Prell, Y. Kyriakou, and W. A. Kalender, "Comparison of ring artifact correction methods for flat-detector CT," *Physics in Medicine and Biology*, vol. 54, no. 12, p. 3881.